

Low-energy electron ionization mass spectrometer for efficient detection of low mass species

Cite as: Rev. Sci. Instrum. **92**, 073305 (2021); <https://doi.org/10.1063/5.0050292>

Submitted: 13 March 2021 • Accepted: 04 July 2021 • Published Online: 20 July 2021

 M. Bergin,  D. J. Ward,  S. M. Lambrick, et al.



View Online



Export Citation



CrossMark

ARTICLES YOU MAY BE INTERESTED IN

[Time-resolved ion energy measurements using a retarding potential analyzer](#)

Review of Scientific Instruments **92**, 073306 (2021); <https://doi.org/10.1063/5.0039621>

[Laboratory plasma devices for space physics investigation](#)

Review of Scientific Instruments **92**, 071101 (2021); <https://doi.org/10.1063/5.0021355>

[Projection-type electron spectroscopy collimator analyzer for charged particles and x-ray detections](#)

Review of Scientific Instruments **92**, 073301 (2021); <https://doi.org/10.1063/5.0051114>



www.amscins.com

3D IMAGING of Ions & Electrons

Perfect replacement for conventional 2D cameras

TPX3CAM READOUT					
ToA (sec)		ToT (nanosec)	Coordinates		
Time of Arrival		Time over Threshold		X	Y
1.134267353184		425	144	140	
1.134267353162		875	57	234	
1.134267353137		875	235	149	
1.134267353120		125	178	140	
1.134267353111		975	5	130	



Low-energy electron ionization mass spectrometer for efficient detection of low mass species

Cite as: *Rev. Sci. Instrum.* **92**, 073305 (2021); doi: [10.1063/5.0050292](https://doi.org/10.1063/5.0050292)

Submitted: 13 March 2021 • Accepted: 4 July 2021 •

Published Online: 20 July 2021








View Online



Export Citation



CrossMark

M. Bergin,^{1,a)}  D. J. Ward,¹  S. M. Lambrick,¹  N. A. von Jeinsen,¹  B. Holst,²  J. Ellis,¹ A. P. Jardine,¹ and W. Allison¹

AFFILIATIONS

¹The Cavendish Laboratory, JJ Thomson Avenue, Cambridge CB3 0HE, United Kingdom

²Department of Physics and Technology, University of Bergen, Allegaten 55, 5007 Bergen, Norway

^{a)} Author to whom correspondence should be addressed: mb802@cantab.ac.uk

ABSTRACT

The design of a high-efficiency mass spectrometer is described, aimed at residual gas detection of low mass species using low-energy electron impact, with particular applications in helium atom microscopy and atomic or molecular scattering. The instrument consists of an extended ionization volume, where electrons emitted from a hot filament are confined using a solenoidal magnetic field to give a high ionization probability. Electron space charge is used to confine and extract the gas ions formed, which are then passed through a magnetic sector mass filter before reaching an ion counter. The design and implementation of each of the major components are described in turn, followed by the overall performance of the detector in terms of mass separation, detection efficiency, time response, and background count rates. The linearity of response with emission current and magnetic field is discussed. The detection efficiency for helium is very high, reaching as much as 0.5%, with a time constant of (198 ± 6) ms and a background signal equivalent to an incoming helium flux of $(8.7 \pm 0.2) \times 10^6 \text{ s}^{-1}$.

© 2021 Author(s). All article content, except where otherwise noted, is licensed under a Creative Commons Attribution (CC BY) license (<http://creativecommons.org/licenses/by/4.0/>). <https://doi.org/10.1063/5.0050292>

I. INTRODUCTION

Detection of low mass species such as helium or hydrogen is essential in many technological and research applications, including ultra-low pressure measurement and leak detection,^{1–3} neutral gas measurements in space,⁴ and monitoring fusion reactions.⁵ Many helium scattering experiments also require very high-efficiency helium detection in order to, for example, observe weak diffraction peaks⁶ or to observe surface correlations using the small number of diffuse atoms that are quasi-elastically scattered.⁷ Similarly, in the emerging field of helium microscopy,^{8–15} narrow beams of helium are required for high resolution images, which, in turn, reduce the flux of helium dramatically,^{16–18} again necessitating sensitive detection.

While helium is valuable as an inert and non-destructive probe, the same characteristics make it particularly difficult to detect. The most common approach is first to ionize the helium and then to detect the ion current. Ions are usually created by electron impact in a defined volume of space, and most commercial

residual gas analyzers use an ionization volume of the order 1 cm^3 . Then, mass selection of the ions may be performed by a quadrupole mass filter and an electron multiplier, leading to a sensitivity of about $1 \times 10^{-4} \text{ A/mbar}$.¹⁹ Depending on the measurement configuration in a typical vacuum system, these give a detection efficiency from 10^{-5} to 10^{-7} for incoming helium atoms.

In general, ionization efficiency can be improved by increasing the size of the ionizer, the electron density inside, and the duration that gas particles spend in that region—provided that the ions formed can still be extracted without significant losses. An established method of achieving these improvements is by using a solenoid magnetic field to confine the trajectories of the energetic electrons,^{20–23} which can also extend the size of the ionization region and constrict the flow of gas through the ionizer. In a previous paper,²⁴ simulations examining the general principles of a solenoid ionizer, including the electron space charge formed inside, and how that can be used to contain and extract the ions formed have been reported.

In the current work, we report the realization of a complete solenoid ionizer based detector system, building on the principles detailed in Ref. 24 and two prototype instruments.^{22,25} The ionizer we report is so efficient that it multiply ionizes atoms such as carbon and oxygen, giving rise to a significant background at both mass-to-charge ratios of $m/z = 3$ and $m/z = 4$, so a key feature of our new instrument is that it operates at an electron energy of only 100 eV, thus limiting multiple ionization while maintaining ionization efficiency. The instrument described here is principally intended for detection of helium atoms in a scanning helium microscope (SHeM);^{10,26} although it can be used much more widely, for example, the same design has been used in hydrogen scattering experiments,^{27,28} allowing a careful study of rotational states during molecule-surface collisions.

The remainder of this paper is organized as follows: A description of the overall design for the high-efficiency detector is given in Sec. II. Each component of the complete detector system is then discussed, starting in Sec. III with the ionizer, then moving onto the mass selector in Sec. IV, and the ion detection in Sec. V. Finally, we describe the key performance metrics, including the detection efficiency, background, and response time in Sec. VI.

II. OVERALL DESIGN

The detector reported here aims to achieve a very high efficiency for detection of low mass species while simultaneously minimizing background on the detected signal and achieving a fast response to changes in the rate of incoming atoms. The overall design cannot be optimized for all these goals simultaneously, so represents a compromise between competing factors. For helium microscopy and similar scattering experiments, the available signal levels typically correspond to a flux of less than 10^8 atoms per second entering the detector, which often need to be measured to a precision of the order 1%,^{13,14} with a time response of a few hundred milliseconds.

Figure 1 shows the three main components that make up the detector both (a) schematically and (b) graphically. The solenoidal ionizer, A, produces ions from residual gas entering via the gas inlet. The mass filter, B, then transmits only selected ions with a particular m/z ratio (usually $m/z = 4$ for He^+ ions), and the ion detector, C, detects and amplifies individual ion arrival events for the electrical measurement. Ion optics are used to transfer the ions from each component to the next without significant loss and incorporate astigmatic focusing and beam manipulation capabilities. The

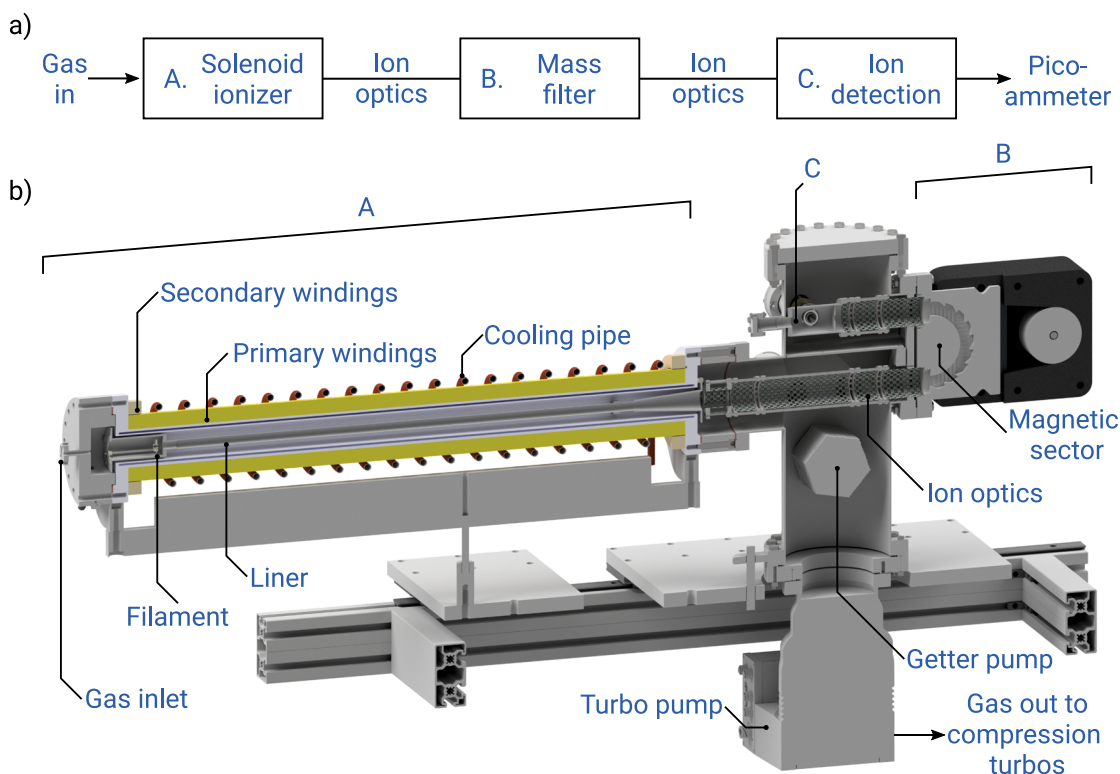


FIG. 1. (a) Schematic representation of the solenoidal ionizer, which consists of three main components (A, B, and C) separated by ion optics. (b) A cross-sectional view of the complete instrument. Helium atoms entering from the left are ionized by electron bombardment (A). Ion optics are used to transfer the ions from the ionizer to a magnetic sector (B) where they are mass selected. Ion optics either transfer the ions to an on-axis Faraday cup (C) or are deflected into a dynode and an electron multiplier (not shown, see Sec. V).

ion detector consists of a conversion dynode and an off-axis channel electron multiplier, as well as an on-axis Faraday cup to measure large signals without multiplication during setup and calibration.

The solenoidal ionizer uses a magnetic field to constrain the motion of electrons emitted from a hot cathode filament, enabling the large ionization volume that is needed to give a high probability of ionizing incoming atoms. Its detailed design is discussed in Sec. III and centers on designing the space charge to trap and extract the ions formed, building on the largely theoretical work of Alderwick *et al.*²⁴ However, in terms of the overall instrument, a key result^{24,25} is that the space charge formed within the ionizer reaches tens of volts, depending on the precise configuration. Ions are subsequently formed in different potential regions within the ionizer; thus, the outgoing ion beam can have a spread of energies of tens of volts or more.

The wide spread of ion energies limits the methods that can be used for mass filtration without significant losses. A 180° magnetic sector was chosen as suitable to accommodate the spread, designed for an incoming ion energy of ~1000 V. For practical convenience, the bending field region was fixed at ground potential, requiring the ions to be formed at a variable elevated potential. The ionizer therefore incorporates a floating tubular “liner,” which provides the necessary electrical boundary condition; ions are formed at a spread of potential energies, slightly below the liner potential, as a result of the electron space charge. Since the liner voltage can then be varied to control the energy of the ions in the magnetic sector and thus the m/z ratio of the transmitted ions, the magnetic sector was implemented using a fixed, permanent magnet.

In our application, the helium flux is small so the detector needs an exceptional rejection probability of background ions. The background signal at a particular m/z ratio is made up of two contributions: stray ions with the incorrect m/z reaching the ion detector and the presence of additional multiply ionized species with the same m/z as He^+ . Both are reduced by reducing the ultra-high vacuum background pressure, so the combination of a turbomolecular pump (Pfeiffer HiPace300M), a large getter pump (Saes Getters CapaciTorr D3500), and a small getter pump at the gas inlet (Saes Getters CapaciTorr CF16-MK2-172-2X16-10, not shown) is used to maintain a pressure in the vacuum chamber holding the ion optics of $< 5 \times 10^{-11}$ mbar during operation. Two further turbomolecular pumps (Pfeiffer HiPace80) back the main turbopump in series to ensure compression and removal of very low partial pressures of helium from the system. The getter pump at the gas inlet acts to reduce the background signal and does not pump helium. To minimize stray ions reaching the counter, the vacuum chamber is split into two parts that avoid line-of-sight and the magnetic sector flight tube is carefully shaped to minimize transmission of incorrect ion beam masses or high-energy neutral species generated by ion impact with the flight tube walls. To avoid generation of multiply ionized species, rapid ion extraction from the ionizer is important, as well as designing the instrument to operate with low electron energies.

During operation, gas to be detected is fed into the detector through the “gas inlet” connection on the left of Fig. 1(b). The internal volume of the region around the inlet and filament is minimized, and the solenoid and liner geometry is chosen so its molecular flow conductance is $\sim 0.7 \text{ l s}^{-1}$. These give a good detection probability as the limited gas flow through the ionizer results in an almost

“stagnated” pressure, while still giving an appropriate time response to changes in the input gas.

III. SOLENOIDAL IONIZER

A. Principle of operation

Electron ionization can be achieved through a variety of implementations, and a detailed discussion including relative merits is presented by Alderwick.²² The application of solenoidal ionizers for atom beam experiments was first demonstrated by DeKieviet *et al.*,²⁰ producing an ionizer with a reported efficiency of $\eta = 7 \times 10^{-3}$. The main benefit of a solenoidal ionizer is that it creates a scalable ionization volume, which proportionally increases the device efficiency.

In the present instrument, electrons are injected into a magnetic field and confined using electric and magnetic fields to create a high electron density so that their space charge affects the local electrostatic potential, as illustrated in Fig. 2. The electrons form helical trajectories in the magnetic field. Two modes of operation are possible, as illustrated in Fig. 2(a). Electrons may be trapped inside the solenoid, closed mode, or can pass directly through the ionizer, open mode. The choice of the operational mode is determined by the electrostatic potential downstream of the solenoid. If the downstream potential is greater than the filament potential, electrons emerge to be collected on a downstream lens element so that the ionizer is in open mode. If the downstream potential is below the filament potential, the instrument operates in closed mode with electrons reflected so that they run up and down the ionizer until they are re-absorbed at the filament or undergo some other loss mechanism.

In a region of high electron density, space charge acts to reduce the local potential. Alderwick *et al.*²⁴ derived expressions for the axial potential inside the solenoid as illustrated in Fig. 2(b). A key result is that space charge creates a potential well that confines any ions radially. The well depth increases with the logarithm of the radius of the electrode confining the electron beam so that the electrode can be engineered to generate the desired axial potential. In the current implementation, a tapered electrode at the exit is used to generate the field needed to extract ions from the solenoid. Similarly, ions are prevented from leaving at the filament end by reducing the radius of the electrode with a ring that acts as a barrier.^{22,25}

Some similarities between the ionizer we employ and other techniques exist, for example, Electron Beam Ion Sources (EBISs) are used to produce bare nuclei of high mass species such as uranium.²³ These ion sources typically generate and subsequently trap ions using electromagnetic fields. The ions are then bombarded with a high electron current to multiply ionize them and produce multiply ionized species with high charge. The electron sources from the technique could be applied to improve efficiency in helium detection presented in the current work, assuming that there is sufficient capacity within the ionizer space charge region to benefit from more efficient electron injection. However, the direct application of the ionizer would not be appropriate, since it would lead to an unacceptably high background signal from other multiply ionized species.

B. Implementation

Figure 3 shows a detailed cross section of the ionizer. The filament is mounted inside the solenoid in front of a repeller

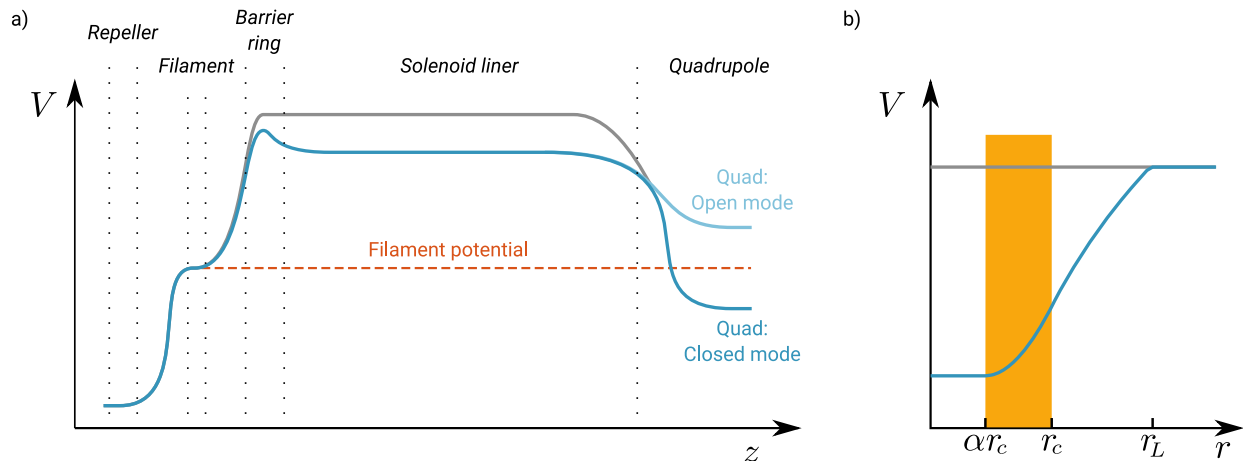


FIG. 2. Electrostatic potential in the ionizer showing how electron space charge is used to trap and extract ions. At typical operating pressures, the ion space charge is negligible compared to the electron space charge. (a) Schematic of the center line potential throughout the ionizer in the two modes of operation (open or closed). The solid gray line shows the potential in the absence of space charge. The solid blue line includes the effect of electron space charge. In open mode, the electrons are collected downstream of the ionizer. In closed mode, electrons are reflected close to the point where the axial potential and filament potential (shown as a dotted red line) are the same. The barrier ring prevents ions leaving the left of the device. It is implemented by the reduction in the diameter shown in Fig. 3. (b) Radial variation of the electric potential, $V(r)$, inside a long solenoid ion source based on Fig. 2 of Ref. 24. The gray line is the potential inside the solenoid without space charge, while the blue line is the potential inside the liner with space charge as given by Eq. (1) of Ref. 24. It is assumed that the electrons form a cylindrical cloud between the shaded regions ($\alpha r_c < r < r_c$).

electrode and close to a transparent grid (wire diameter of 0.001 in., 40 wires/in. and an open fraction of 92.2%) at the mouth of the ionization region (liner). Electrons are generated by thermionic emission from a heated iridium filament with a diameter of about 200 μm coated in thoria. Thoria coating lowers the work function

at the surface, allowing similar electron emission currents to be obtained at lower cathode temperatures,²⁹ reducing localized heating and gas release in the region. The precise position of the filament influences the electron trajectories in the solenoid and, therefore, changes the performance of the ionizer.²⁴

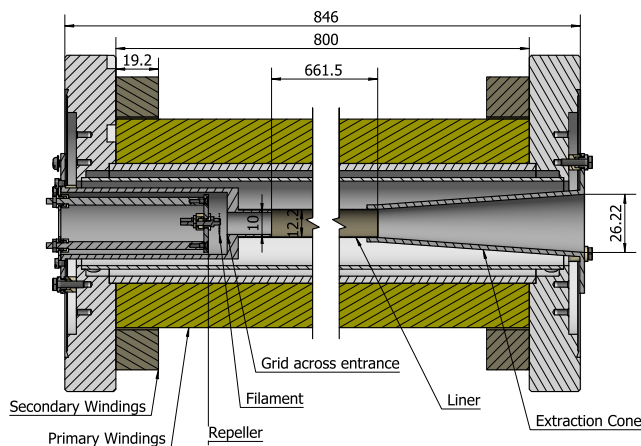


FIG. 3. Cross-sectional view through the solenoid and ionizer showing key components and dimensions in mm. The filament is mounted so that it is inside the solenoid and close to the grid at the entrance to the confining electrode (liner). Long metal rods support the filament from the liner and ceramics are used to insulate the filament mount from the liner. Extraction of ions to the left is inhibited by reducing the bore of the confining electrode (liner) from 12.2 to 10 mm [see Fig. 2(a)]. The extraction cone is created by tapering of the confining electrode (liner) as shown at the right. The solenoid windings are made up of a uniformly wound primary winding together with two rectangular-section secondary windings that act as correcting coils.

The electron trap and ionization volume consists of a double wall vacuum vessel through which cooling water may be introduced; onto that is wound a primary winding consisting of ten layers of $3.0 \times 2.0 \text{ mm}^2$ rectangular section wire with additional secondary coils made of nine layers of $3.0 \times 2.0 \text{ mm}^2$ rectangular section wire. The wire is mechanically wound and encapsulated using boron nitride loaded electrical varnish (70% Utmeg U2000L 27% boron nitride powder 3% silica flour) for improved thermal conductivity away from the winding; the addition of silica flour makes the mixture thixotropic for no-drip application. After curing, the complete assembly is wound with additional external water cooling pipes applied using Duralco 2-part thermally conducting epoxy.

The (liner) electrode surrounding the electrons is electrically insulated from the vacuum vessel using insulating posts at either end of the assembly. The front of the liner contains a wide section for mounting the electron source as shown in Fig. 3, and at the exit, the tube tapers to form an extraction cone, as discussed previously. The liner is connected to an electrical feedthrough at each end; during commissioning, a large current ($\sim 25 \text{ A}$) can be passed through the tube, heating it to $\sim 400 \text{ C}$ to accelerate desorption of gas from the liner wall to reduce the presence of background gases. During operation, the liner can be attached to a high voltage power supply, which defines the ion energy for ions generated in the ionizer.

C. Measured emission characteristics

The emission characteristics of the filament are as expected. Emission increases with the filament current and with the electron

energy, the emission being dominated by space charge effects at low energies (~ 50 V). The repeller has relatively little impact on the emission current, provided it is negative with respect to the filament.

It is possible to switch between open and closed modes of the ionizer by changing the electron energy or the potential downstream of the ionizer, which acts as an extraction voltage for ions. The transition between open and closed modes occurs close to the point where the electron energy is equal to the extraction voltage (see Fig. 2). Figure 4 shows the effect of changing from closed to open mode on the electron currents in the ionizer. At low extraction voltage (left of the plot), electrons cannot escape the ionizer and it operates in closed mode. All of the current emitted by the filament (blue data points) is collected by the liner (orange data points). At higher extraction voltages, the device switches to open mode and the vast majority escape so that the liner current decreases. An insignificant current is measured onto the liner in open mode, implying that the electrons are successfully transferred through the entire solenoid by the magnetic field.

Changes in the electron distribution have a direct effect on the ionization efficiency. Figure 5 shows how the measured ion current changes as the operating mode is switched from closed (left) to open (right). Here, the change is generated by varying the electron energy and a sharp decrease in efficiency of the detector is observed when the ionizer switches to open mode. The measurements confirm that there is a distinct difference between the two operating modes of the

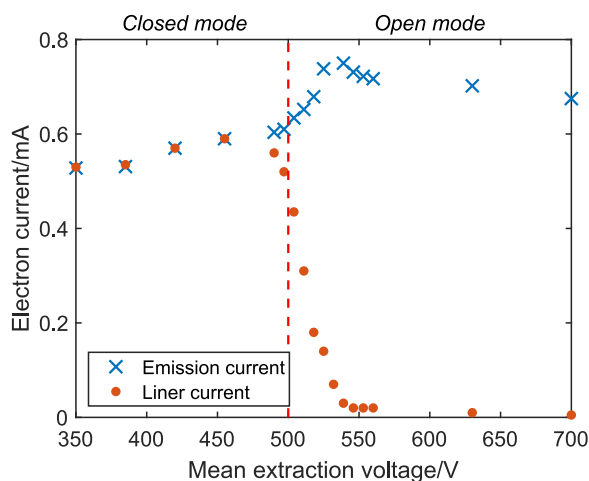


FIG. 4. Electron current variation as the ionizer is switched between closed mode (left) and open mode (right). The blue data points show the current leaving the filament, and the orange data points show the current collected on the confining electrode (liner). The mode is switched by varying the voltage downstream of the ionizer, thus giving an extraction voltage (x axis). The vertical dashed line indicates the point at which the filament voltage and the extraction voltage are the same. To the left of the dotted line, electrons have insufficient energy to escape and are trapped in the ionizer (closed mode); to the right of the dotted line, electrons can escape from the ionizer (open mode). In closed mode, the filament emission current is identical to the current arriving on the liner, as expected. In open mode, the electrons pass straight through the solenoid and the current onto the liner drops to approximately zero. Details on how the electron currents were measured can be found in Fig. 8. The data shown here and in Fig. 5 use an older filament mounting, but the behavior is qualitatively the same as the arrangement shown in Fig. 3.

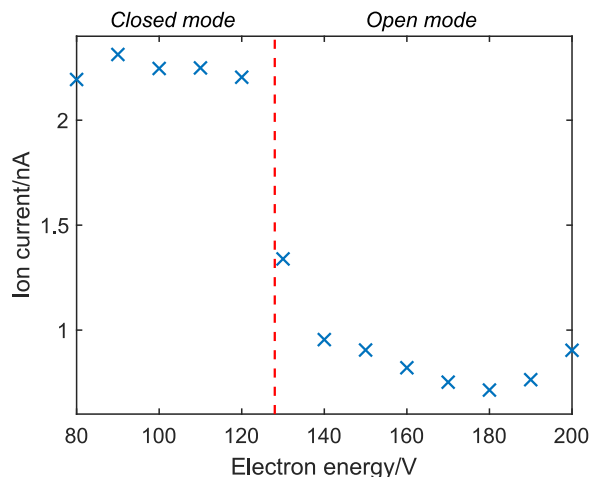


FIG. 5. Ionization efficiency, measured as an ion current, in closed mode (left) and open mode (right). Here, the electron energy (x axis) is varied to switch between closed and open modes while maintaining the downstream extraction voltage constant. The vertical dashed line indicates the point at which the transition from closed to open is expected. At low energies, the electrons have insufficient energy to emerge from the ionizer, and it operates in closed mode; at high energies, the electrons escape, and it operates in open mode. Significantly, more ions are generated in the closed mode.

detector due to the higher electron density in the ionizer in closed mode.

IV. MASS FILTERING AND ION OPTICS

A. Principle of operation

Once the ions have been extracted, they are separated by mass to reduce the signal from background gas in the vacuum system. Most residual gas analyzers use quadrupole based mass filters,^{1,30} which are typically suitable for analyzing ions with a low kinetic energy (≤ 10 eV). In the present application, the mass analyzer must cope with a significant spread of ion energies due to the deep space charge well in the ionizer [see Fig. 2(b)]. As a result, we use a magnetic sector, operating with ion energies of several hundred electron volts, to perform the mass analysis.

Our implementation uses a permanent magnet to generate the field in the bending region and tunes the mass-to-charge ratio selection by varying the ion energy. The kinetic energy of the ions is supplied from acceleration of the ions out of the ionizer to the ground potential of the chamber. If the liner is at a potential V , the kinetic energy of the ions will be $(1/2)mu^2 = qV$. By equating the Lorentz force, $\vec{F} = q(\vec{E} + \vec{u} \times \vec{B})$, experienced by the ions moving through the uniform magnetic field, B , to the centripetal force needed to produce circular motion, $F_{CM} = mu^2/R$, it can be shown that the ions will perform circular motion with a radius of curvature, R , given by

$$R = \frac{1}{B} \sqrt{\frac{2mV}{q}}. \quad (1)$$

Therefore, only ions with the desired mass-to-charge ratio will pass through without colliding with the curved chamber wall, providing mass filtering.

B. Magnet design

The sector magnet consists of a yoke and pole pieces made of soft iron (minimum iron content of 99.85%, known as Remko, Armco, or Maximag) driven by a cylindrical permanent magnet made of N42 neodymium-iron-boron alloy (NdFeB). The permanent magnet is a readily available commercial unit (first4magnets F4M20103) with a diameter of 80 mm and a length of 65 mm. It is prefabricated as a hollow NdFeB cylinder with the remainder being ferritic stainless steel and the whole cylinder is encased in 2 mm of 316 stainless steel. After assembly, the yoke has a gap of 15 mm to fit over the vacuum flight tube.

The inset to Fig. 6 shows a cross section through the yoke and permanent magnet. At the entrance to the pole piece, the yoke is shaped to reduce the fringing field in the region outside the gap while ensuring that the yoke material does not saturate. The main panel in Fig. 6 shows simulated and measured fields in the gap region. Blue crosses give the measured field and the orange curve shows the field simulated in Lorentz³¹ assuming an ideal, uniformly magnetized cylinder of neodymium. The simulation and measurements confirm that the field is highly uniform inside the gap and that the field drops away rapidly outside the gap. The difference in magnitude between the simulation and measurement is consistent with the approximate geometry of the permanent magnet used in the simulation, given the real magnet is not a uniform cylinder of neodymium.

The magnet assembly is shown in the cross section in Fig. 1(b) together with the flight tube (labeled magnetic sector in the figure). Secondary ions and energetic neutral species are generated in the flight tube when ions having the incorrect m/z ratio strike the walls of the tube. To minimize background from the secondary particles,

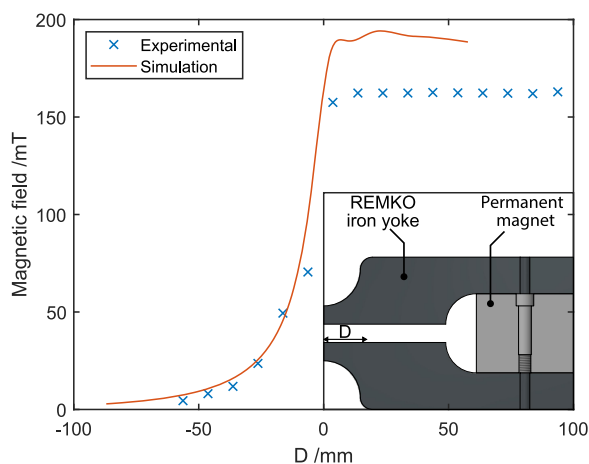


FIG. 6. (Inset) Cross-sectional view of the magnetic sector taken in a plane parallel to the field. The permanent magnet is lightly shaded on the right of the figure and the soft iron yoke is shown in a darker shading. (Main figure) Measured (blue crosses) and simulated (orange line) values of the magnetic field along a line containing both planes of mirror symmetry. The distance, D , is measured from the pole piece edge. Measurements and simulation confirm the uniformity of the field within the gap of pole pieces and the rapid drop in field outside the pole pieces. Differences between the simulation and the measurement are attributed to a lack of uniformity in the permanent magnet.

internal surfaces of the flight tube are machined with serrations [see Fig. 1(b)].

C. Ion optics design

Electrostatic lenses transport ions from the ionizer to the entrance of the mass selector and from the exit of the selector to the detector. The lenses accelerate ions to an energy suitable for mass selection and provide correction for the astigmatism of the magnetic sector. The magnetic sector is mounted externally to the vacuum chamber (Fig. 1), and the geometry of the ion optics is therefore dictated by the dimensions of the chamber. The magnetic sector is at ground potential so that the ion energy is determined by the potential applied to the liner of the ionizer, HT1 (see Fig. 8). A lens with quadrupolar geometry corrects for the astigmatism of the magnetic sector³² and provides for beam steering to accommodate any mechanical misalignment.

The lens stack between the ionizer and the mass selector consists of five elements. The first three elements include the quadrupole element and accelerate the ions to the desired energy (ground potential), while the remaining elements act as an einzel lens to transport ions to the selector entrance. The lens stack at the output of the selector is another einzel lens.

The two lenses leading from the ionizer to the mass selector use focusing voltages that accelerate the ions into the lens (negative with respect to the mass selector), leading to a smaller chromatic aberration. However, on the exit to the mass selector, we use a focusing voltage that decelerates the ions as they enter the lens (positive with respect to the mass selector). The aim here is to increase chromatic aberrations so that secondary ions are more strongly defocused, while secondary electrons from stray particles that strike the lens element are prevented from reaching the ion detector (Sec. V). In this way, the background is significantly reduced.

Figure 7 shows LORENTZ³¹ simulations for trajectories of the ions up to the exit from the magnet. It can be seen that the masses are well separated in space. The simulation shown in Fig. 7 has a transmission probability of 40%, between the ionizer and the magnet exit. Most losses arise from ions deviating from the plane of the magnetic sector and striking the wall of the magnet housing.

The details of the assembly procedure can be found in Bergin's Ph.D. thesis;²⁶ in particular, images of the assembled ion optics and the support structure can be found in Fig. 4.22.

D. Power supplies

The system is controlled by a series of programmable power supplies with typical working values shown in Table I. The power supply configuration is illustrated in Fig. 8. Most supplies are single polarity and ground referenced. The filament and electron energy float with respect to the liner, HT1, as shown in the inset of Fig. 8. The emission current is regulated by incorporating the filament supply in a proportional integral differential (PID) loop controlled by a Linduino micro-controller with the emission current measured internally by the electron energy supply, HT0.

The control system for the power supplies includes the ability to scale the ion-optical voltages (columns 2 and 3, Table I) of lenses automatically as the nominal ion energy, HT1, is changed. Similarly,

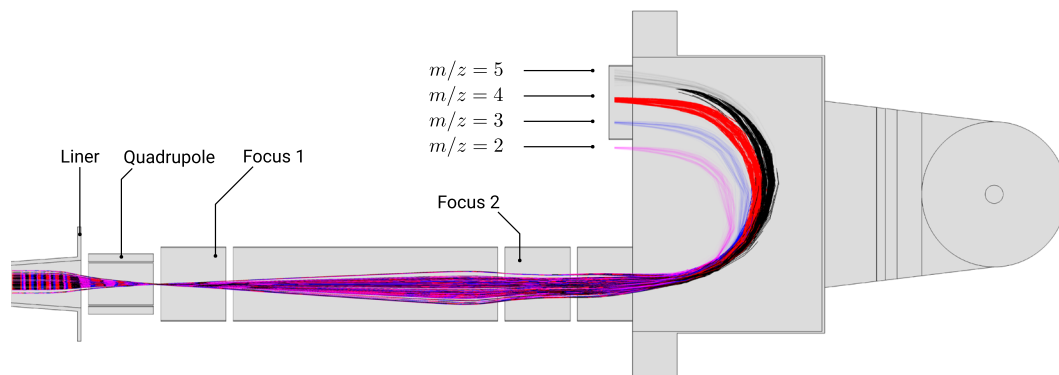


FIG. 7. Simulation of ion optics to transfer the ions from the ionizer to the magnet and then subsequent mass filtering. The magnetic field is calculated from a 3D model of the permanent magnet, but as shown in Fig. 6, the steady field is overestimated (corrected in practice using as slightly adjusted liner voltage). Note that the flight tube was not included in the simulation, so in reality trajectories that deviate from the 50 mm semicircle through the magnetic sector will collide with a wall and be removed and are illustrated as translucent in the figure. Some elements were not included in the simulation due to changes in design during implementation; the lens on the ion optics stack immediately following the magnet and the dynode assembly are not included, and in the top ion optics stack, the lens dimensions have been adjusted in assembly.

the repeller voltage, HT11, is automatically scaled to maintain a constant field around the filament as the ion energy is changed. The user interface provides intuitive controls, such as the quadrupole mean energy, V_q , the quadrupole voltage difference, δV_q , and the

left/right and up/down pusher voltages, δV_{lr} and δV_{ud} , from which the supply voltages are calculated and scaled.

TABLE I. Typical operating values for the detector optimized for the detection of He_4^+ in helium microscopy. Descriptive labels and corresponding power supply designations (see Fig. 8) are in the left column. Typical values (col. 2) are those produced by the power supplies, most of which are referenced to the laboratory ground. Ion optical potentials (col. 3) are referenced to the notional zero of kinetic energy for the ions for which we have assumed an axial space charge of 50 V in the liner of the ionizer (Fig. 8). Potentials on the quadrupole elements are expressed as the mean potential, V_q , the quadrupole voltage difference, δV_q , and the left/right and up/down pusher voltages, δV_{lr} and δV_{ud} . The final column expresses the ion-optical voltages as a ratio to the ion energy at laboratory ground where the mass selection takes place ($V_i = 650$ V in the case shown).

Module name	Typical value	Ion-optical potential	V/V_i
Electron energy (HT0)	-100 V		
Ion energy (HT1)	725 V		
Repeller (HT11)	525 V		
Quadrupole left (HT3)	562 V	$V_q = 110$ V	0.16
Quadrupole right (HT4)	555 V	$\delta V_q = \pm 7.3$ V	0.01
Quadrupole up (HT5)	574 V	$\delta V_{lr} = \pm 0.73$ V	0.001
Quadrupole down (HT6)	572 V	$\delta V_{ud} = \pm 3.6$ V	0.005
Focus 1 (HT7)	-1890 V	$V_{F1} = 2560$ V	3.8
Focus 2 (HT8)	-2030 V	$V_{F2} = 2710$ V	4.0
Focus 3 (HT2)	566 V	$V_{F3} = 110$ V	0.16
Dynode (HT9)	-3000 V	$V_d = 3675$ V	5.4
Channeltron (HT10)	-1300 V		
Filament	3 A		
Emission	1 mA		
Main solenoid	20 A		
Secondary winding	35 A		
Chamber pressure	$< 10^{-10}$ mbar		

V. ION DETECTION

The instrument includes two detectors, as indicated in Fig. 8. For high ion currents, a Faraday cup placed on the axis provides an absolute measure of the ion signal, while, at lower ion currents, the currents are amplified using an electron multiplier. Injecting ions directly into a channel electron multiplier is known to reduce lifetime through the effects of ion sputtering.³³ Here, we employ a discrete dynode to convert ions to electrons before injection into the electron multiplier. The design allows an off-axis arrangement that eliminates line-of-sight for energetic neutral particles and reduces unwanted background.^{25,33}

The dynode differs from those of a scintillator/photomultiplier ion detector,³⁴ where high voltages, greater than 10 kV, are necessary. Here, we use lower voltages (~ 3 kV), which are simpler to manage while giving significant secondary electron emission^{35,36} and high detection efficiency. The dynode has a concave, spherical surface to focus the low-energy electrons into the mouth of the multiplier. Figure 9 illustrates the principle.

The spherical surface has two effects on the secondary electrons; first, they will be directed toward the multiplier through geometric effects. The normal to the surface always points toward the multiplier, and since the electrons are emitted with a cosine distribution,³⁷ they are generally emitted in the direction of the surface normal. The second effect the curved dynode has is that the electric field will also point along the surface normal, so electrons are accelerated toward the multiplier once they have been emitted. By using a large voltage on the dynode, it is possible for the initial acceleration from the dynode to overwhelm the repulsion at the multiplier.

The physical size of the dynode is much larger than that of the beam to create a uniform field for accelerating the secondary electrons and avoid fringing fields at the boundary between the dynode and the ground case. An aperture is used to shield the ions from the strong field until they enter the dynode assembly to ensure that the

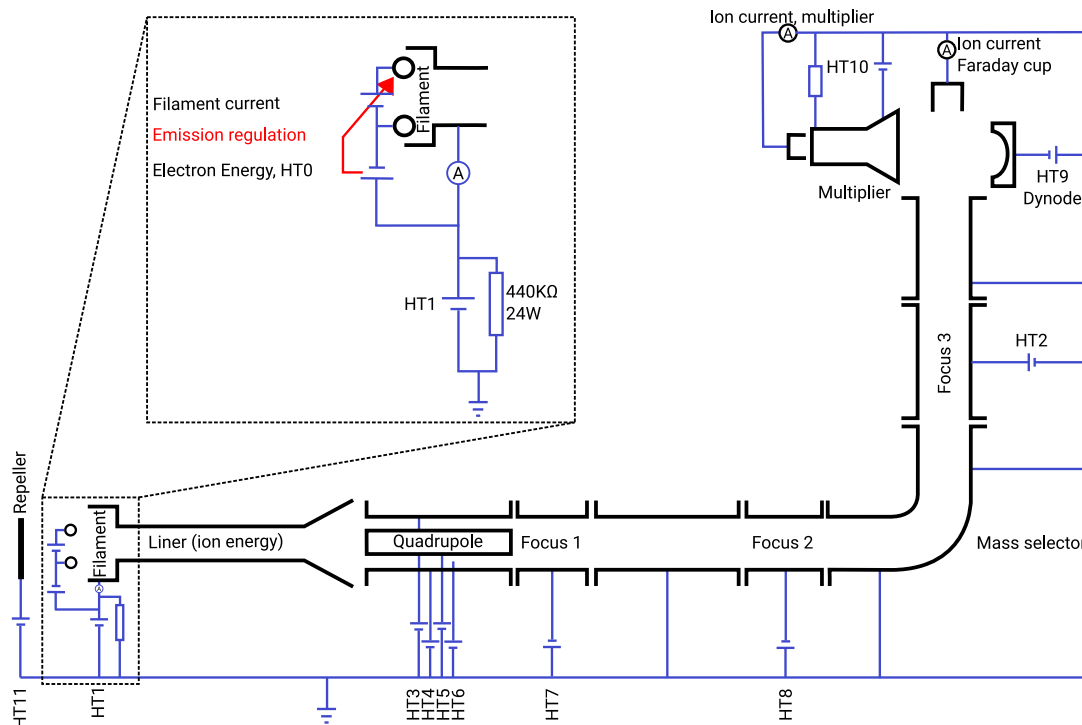


FIG. 8. Power supply schematic illustrating how the electrical components in the detector are connected. Most power supplies are referenced to laboratory ground except for the filament and electron energy, HT0. A 440 k Ω resistor is connected across the liner (ion energy) supply, HT1, to provide a return path for electrons collected on elements other than the liner. The voltage across the electron multiplier is determined by HT10 and a series resistor. Together with the internal resistance of the multiplier, the resistor acts as a voltage divider to generate an extraction field for electrons leaving the multiplier. Ion currents can be measured with ground-referenced pico-ammmeters at either the Faraday cup or at the collector of the multiplier. Note that of the three focus electrodes, Focus 1 and Focus 2 are negative voltages so that the ion energy is increased within the lens. Such lenses have lower chromatic aberration than the configuration used for Focus 3, where the ion energy is reduced in the lens. We employ the higher chromatic aberration of the output lens (Focus 3) to both prevent electrons generated from collisions on the lens reaching the dynode and as an additional filter to discriminate against ions scattered inelastically from the walls of the magnet housing. The total emission current is measured through the supply HT0, while the electron current onto the liner shown in Fig. 5 was measured by floating an ammeter at the position shown in the inset.

ions strike the center of the dynode. Aluminum was chosen as the material for the dynode due to its good yield of secondary electrons, low sputtering yield, and ease of manufacture.

A. Simulated performance of the dynode

IES LORENTZ³¹ was used to simulate the behavior of charged particles in the dynode assembly. Helium ions traveling parallel to the optic axis enter the simulation with a width of 10 mm and an initial energy of 700 V to match the pass energy through the magnet for helium in Fig. 12. At each position where an ion strikes the dynode, secondary electrons are released and the trajectories of these electrons are simulated. A MATLAB script takes the positions where the ions strike the dynode and generate secondary electrons having a Gaussian energy distribution ($E_e > 0$) with the mean and standard deviation of 4 eV³⁷ and a direction sampled from a $\cos \theta$ distribution.³⁸

Figure 9 shows examples of helium ion and electron trajectories in the dynode assembly. The helium ions are plotted as blue lines and are deflected by the large negative voltage on the dynode. The red lines are the generated secondary electrons, and these are pushed onto the electron multiplier by the same field that

deflected the helium ions. In Fig. 9, 99.3% of the electrons reach the multiplier entrance, indicating correct operation.

B. Mechanical design

Figure 10 shows a rendered cross-sectional view of the dynode and its insulators, where the sides of the aluminum dynode are replaced with PEEK to provide an insulating surface to mount the dynode to the grounded case. To reduce the possibility of surface conduction, grooves and raised sections were added to the PEEK.³⁹ Figure 10 also shows how the cylindrical case contains a 10 mm aperture to shield the incoming ions from the dynode field. More detailed images of the mount for the multiplier can be found in Figs. 4.33 and 4.36 of Ref. 26. The multiplier assembly is mounted on a separate feedthrough and can be replaced as a unit.

Measurements and simulations showed that the entrance cone of the multiplier must be screened from external electric fields. A mesh with a wire diameter of 0.001 in., 40 wires/in., and an open fraction of 92.2% was attached to the front of the multiplier using a circlip with a 16 mm external diameter (Accugroup P/N HEC-16-A2).

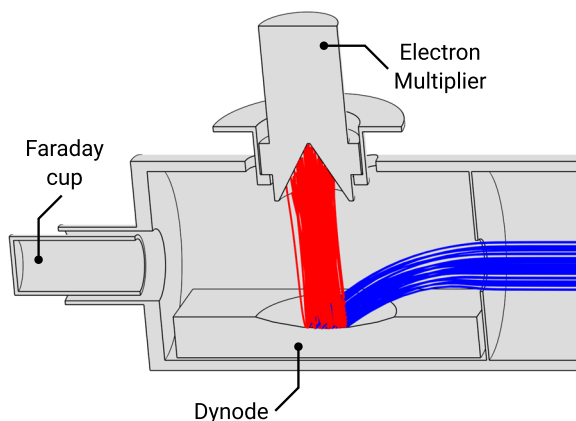


FIG. 9. Simulated trajectories of helium ions and secondary electrons inside the dynode assembly. The blue lines indicate the trajectories of helium ions, while the red lines indicate the trajectories of the secondary electrons. In this simulation, the dynode has a voltage of -2500 V, the electron multiplier has a voltage of -1300 V, and the remaining surfaces are at ground.

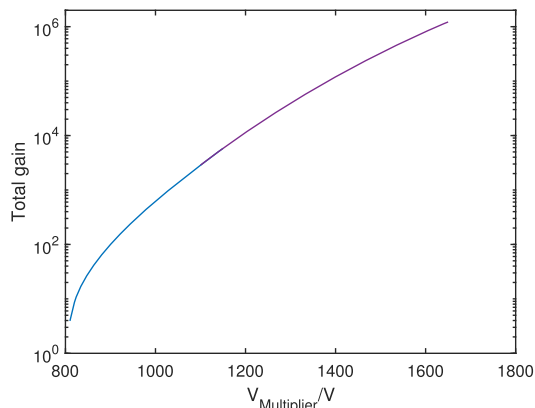


FIG. 11. Gain of the dynode and multiplier as a function of the voltage applied to the front of the multiplier (HT10). The total gain is defined as the ratio of the electron current leaving the multiplier to the incident ion current striking the dynode. At low gain (blue line), the incident ion current was measured directly using the Faraday cup. At high gain (purple line), the number of incident ions is reduced, to avoid saturating the multiplier, and a direct measurement of the incident current is impossible. The high-gain data are normalized to the low-gain region in the regime where they overlap.

C. Performance

The gain of the dynode and multiplier assembly was measured by comparing the electron current at the multiplier output with the ion current arriving at the dynode. The latter was measured, at low multiplier gain, using the Faraday cup (Fig. 9). Figure 11 shows the dependence of the gain on the voltage applied to the multiplier. Measurements at higher gain necessitated smaller incident ion currents, and the data in that regime are normalized to low gain data in the region of overlap.

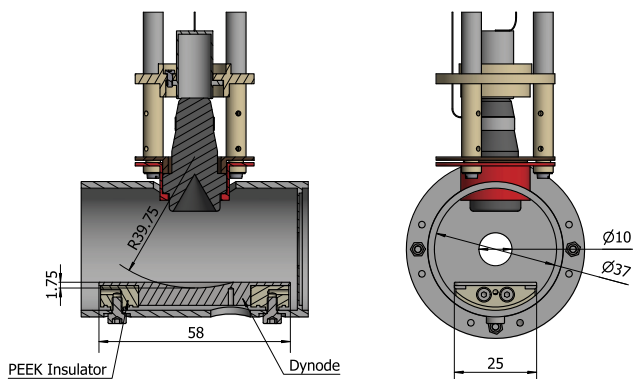


FIG. 10. Cross-sectional view of the full dynode assembly illustrating the dynode, the insulating PEEK components, and how the dynode is attached to the cylindrical case. The dynode has a spherical dip machined into it to improve the performance. The PEEK insulators, as seen in a beige color, can be seen to have a series of raised section and grooves to increase the linear distance between the dynode surface and the grounded case. The electron multiplier is assembled on a separate feedthrough and protrudes into the dynode case as seen in the figure. The red and brown top hat metal pieces on the left of the diagram are pinched together to hold the electron multiplier in place and make an electrical connection. The curvature of the dynode is illustrated to show how the electrons are pushed toward a point inside the multiplier.

VI. OVERALL PERFORMANCE

A. Mass filtering

Figure 12 shows typical mass scans, using a logarithmic scale for the current. The blue data points show peaks from the background gas, while red data points show results with a small partial pressure of helium in the ionizer. The ion energy is scanned to allow transmission of different masses by the fixed field of the permanent magnet. Peak positions are within 12% of expectation based on an idealized field of flux density 162 mT and radius of 50 mm. In the spectrum of the background gas, peaks are evident at all masses even though the total pressure is extremely low (note the logarithmic scale on the y-axis).

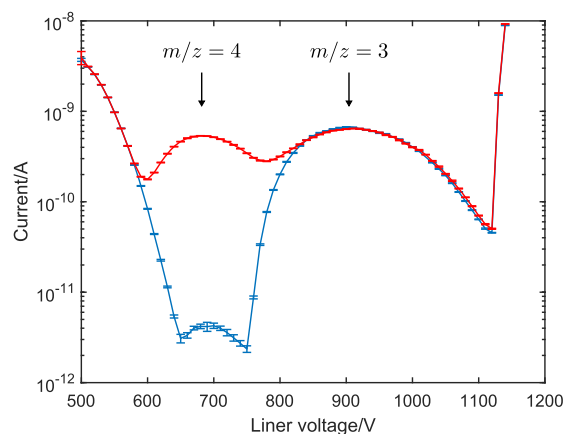


FIG. 12. Demonstration of mass separation showing two mass scans with (red) and without (blue) a helium leak into the detector. The mass 4 peak appears around 700 V and increases in size when the helium gas is bled into the system. Typical operating conditions correspond to the values given in Table I.

The peak at $m/z = 3$ arises from singly ionized HD, a natural isotope of H_2 . The abundance of deuterium in the vacuum chamber can be estimated from the accepted “absolute” mole fraction of deuterium to hydrogen atoms from a single natural source, $\alpha_D = 0.000\,155\,74(5)$.⁴⁰ Ignoring differences in secondary electron yield between different isotopes, the natural abundance of HD is estimated to be $2\alpha_D \approx 0.028\%$.

The natural abundance of D_2 is α_D^2 . Therefore, the ratio of the $m/z = 3$ to $m/z = 4$ peaks is expected to be $2/\alpha_D = 12\,842 \pm 4$. However, it can be seen in Fig. 12 that the $m/z = 4$ peak is about two orders of magnitude larger than what would be expected from just D_2 . Either the secondary electron yield for each isotope strongly varies or an additional component contributes to the background at $m/z = 4$. Sources of background are discussed in more detail in Sec. VI C.

The dip in intensity between the $m/z = 3$ and $m/z = 4$ peaks, together with the rapid attenuation of the $m/z = 3$ peak, suggests that, in this mass region, the signal leakage is negligible (less than 10 ppm).

B. Efficiency

The ionization efficiency is defined as the number of ions generated per incident atom \dot{N}^+/\dot{N} , where both numbers are to be regarded as a flux of particles passing through the ionizer per unit time. We measure the efficiency by leaking gas into the front of the detector, measuring the gas flux at the back, and comparing the flux to the ion current obtained on the Faraday cup. The gas flux through the ionizer can be measured from the pressure and pumping speed next to the pump. The flux of helium down the ionizer Q is given by

$$Q = p_b S, \quad (2)$$

where p_b is the partial pressure of helium and S is the pumping speed at the back of the ionizer. The pumping speed of the Pfeiffer HiPace 300M pump for helium is $S = 2151\text{ s}^{-1}$. We can also express the gas flux Q as the number of atoms passing through the ionizer using

$$Q = \dot{N} k_B T, \quad (3)$$

where \dot{N} is the number of atoms passing through the ionizer per second, k_B is the Boltzmann constant, and T is the temperature of the ionizer. By rearranging Eqs. (2) and (3), we find that the number of atoms \dot{N} passing through the ionizer per unit time is given by

$$\dot{N} = \frac{p_b S}{k_B T}. \quad (4)$$

The rate of ions that are detected is given by

$$\dot{N}^+ = \frac{I \Delta t}{e}, \quad (5)$$

where I is the ion current and e is the electron charge. The efficiency of the ionizer is then defined as \dot{N}^+/\dot{N} , which is the fraction of ions produced from the incoming atoms. The efficiency is

$$\frac{\dot{N}^+}{\dot{N}} = \frac{k_B T}{e S} \frac{I}{p_b}, \quad (6)$$

$$= 1.19 \times 10^{-3} \frac{I}{p_b}, \quad (7)$$

at $T = 298\text{ K}$, where the current I is measured in amps and the pressure at the back of the ionizer p_b is measured in mbar.

Figure 13 shows an example of the efficiency for ^4He measured using the Faraday cup and plotted as a function of the filament current (and, therefore, the emission current). It can be seen that the efficiency varies in a complex way. At low filament current ($I_f < 2.3\text{ A}$), there is a continuous rise in efficiency after the onset of electron emission. The emission current at $I_f \approx 2.3\text{ A}$ is typically 0.2 mA and, above that value, there is a dramatic fall in efficiency to a regime where it is roughly constant but has erratic fluctuations from point to point. The distinction between the low-current and high-current regimes may be attributed to the effects of space charge. At high currents, space charge dominates the behavior and the behavior is correspondingly complex, as has been noted previously.^{41,42} Even so, it is possible to find operating regimes with a high efficiency that are stable. Efficiencies as high as 0.35% have been measured using the Faraday cup and, by scaling the acceptance apertures, we estimate values of 0.5% using the dynode.

Further evidence that the operating mode and the observed efficiency are strongly affected by space charge can be seen by varying the spatial profile of the magnetic field using the secondary winding at the exit of the ionizer (shown in Fig. 3). Typical results are presented in Fig. 14. Here, the efficiency is plotted as a function of currents in both the primary winding (main current) and the secondary winding (secondary current). Figures 14(a) and 14(b) correspond to different values of the filament current. In Fig. 14(a), $I_f = 2.8\text{ A}$ and the emission current $I_e \approx 4\text{ mA}$, while in panel (b), the currents are larger, with $I_f = 3\text{ A}$ and the emission current $I_e \approx 8\text{ mA}$, so the space charge is significantly more important in the latter case. The secondary windings are designed to generate a uniform field along the axis when operated at the same current as the primary winding (main current); however, there is no evidence in the figure that equality of the primary and secondary currents offers any advantage. At higher levels

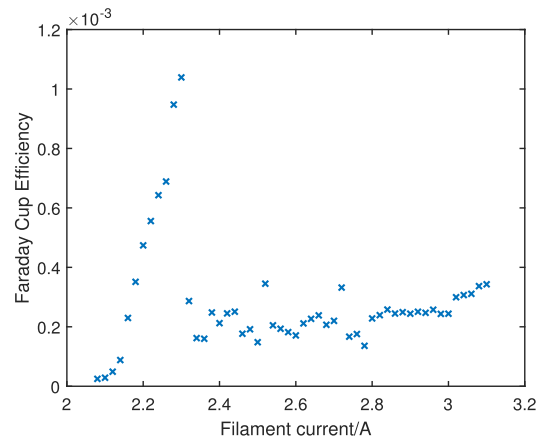


FIG. 13. Measurements of ionization efficiency as a function of the filament current. The ion current is measured using the Faraday cup, leading to an absolute value for the efficiency. The data fall into two regimes: above and below $I_f \approx 2.3\text{ A}$ (see the text). The data were obtained with a current of 10 A in the main solenoid. The scatter in the data points, most noticeable in the regime of high filament current, reflects the complex interaction between electron- and ion-space charge within the instrument (see the text).

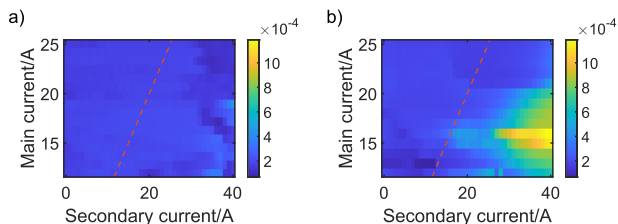


FIG. 14. Measured efficiency as a function of the solenoid current and the current in the secondary winding. The current in the secondary windings changes the uniformity of the axial field and the dashed orange line indicates when the main current and secondary current are equal, giving a maximally flat axial field (a) with a filament current, $I_f = 2.8$ A. Little structure is seen in the data until reaching larger currents in the secondary winding where a small decrease in efficiency is observed. (b) With a filament current, $I_f = 3$ A. A clear peak can be seen at larger currents in the secondary winding.

of space charge [Fig. 14(b)], there is clear evidence that larger currents in the secondary winding at the exit of the ionizer lead to improved efficiency. Increasing the secondary current compresses the electron bundle, leading to the lowering of the axial potential and an increased extraction field for the ions, which may explain the observed behavior. Another instrument that provides an extraction field through the entire volume using an axially varying magnetic field could help understand the effect of the space charge.^{25,43}

For comparison, a typical commercial instrument¹⁹ being pumped at 1 l s^{-1} would have a detection efficiency of order $\eta = 2 \times 10^{-6}$. Other solenoid instruments^{20,44} report higher values than the commercial instrument, but it is difficult to make a direct comparison without a complete parameter set.

C. Sources of background

In the absence of helium gas, the signal output determines the background and hence the minimum signal/noise ratio in the instrument. Several features have been included to minimize the background in the region of mass 4. First, the amount of helium gas reaching the ionizer by back-streaming through the vacuum pumps is minimized by having two types of turbomolecular pumps in series: a Pfeiffer HiPace 300M pump with a compression ratio of $> 10^8$ is backed by a Pfeiffer HiPace 80 with a compression ratio of 1.3×10^7 . A further Pfeiffer HiPace 80 was added and there was no further difference to the background. Second, stray ions and high-energy neutrals are prevented from reaching the detector by careful screening of the detector itself; the inclusion of an electrostatic screen between the upper and lower ion-optic assemblies; and the use of a serrated surfaces inside the spectrometer flight tube (see Sec. IV B).

The remaining background signal will contain contributions from multiple ionized atoms. Figure 15 presents how the ratio of the $m/z = 4$ to $m/z = 3$ peaks varies with electron energy, illustrating how the background signal strongly depends on the electron energy used. Therefore, the detector is operated with an electron energy of about 100 eV to minimize the background at $m/z = 4$. Two multiply ionized atoms that have a mass-to-charge ratio of $m/z = 4$ are O^{4+} and C^{3+} . The cross sections of the ions have not been experimentally measured⁴⁵ but have been theoretically calculated.⁴⁶ The threshold energy for the production of C^{3+} , which is given by the sum of the first three ionization energies, is $E_C = 83.5$ eV, while the threshold

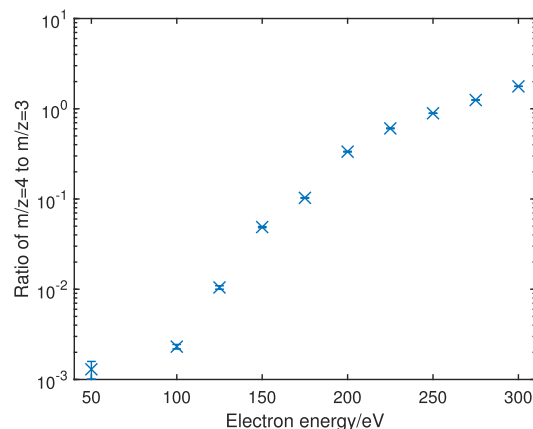


FIG. 15. Plot showing the peak ratio of mass 4 to mass 3 while changing the electron energy. Below electron energies of 150 V, the electron multiplier voltage had to be increased since the total efficiency was dropping. The peak ratio dramatically falls below about 200 eV and continues rolling off until about 100 eV.

energy for O^{4+} is given by $E_O = 181$ eV.⁴⁷ It therefore seems reasonable that at least one of these multiply ionized species contributes to the background at higher electron energies. At lower electron energy, we cannot rule out contributions from D_2 .

After calibrating the efficiency, we measured the background and estimated that it is equivalent to approximately $(8.7 \pm 0.2) \times 10^6$ helium atoms per second entering the detector.

D. Time response

The response time of the detector assembly determines the minimum wait time between independent data points and, when acting as a stagnation detector, it contributes to the efficiency of the detector.^{26,48} It is therefore essential that the time constant is known so that the image noise, acquisition time, and pixel bleeding artifacts can be minimized.

The time response of the detector, when installed on a scanning helium microscope,¹⁰ was measured by moving the beam over a sharp edge between two uniform regions. The response, averaged over 20 measurements, is shown in Fig. 16 (blue curve), together with an exponential function (red curve) that interpolates between the initial and final levels. The exponential time constant we obtain is $\bar{\tau} = (198 \pm 6)$ ms. Contributions to the response other than the ionizer are negligible. For example, the time taken for the microscope to scan across the edge is ≈ 1 ms and makes a negligible contribution to the response of the ionizer. Similarly, the step response of the electrometer used (RBD 9103 picoammeter) to measure the ion current is ≈ 70 ms, which only contributes 6% to the final result.

We have modeled the diffusion of gas from the microscope through the ionizer.²⁶ Details of the calculation can be found on Zenodo.⁴⁹ The simulation results show that the time constant for diffusion is $\tau_s = (241.16 \pm 0.11)$ ms, which overestimates the measured result by $\approx 18\%$. The good qualitative agreement indicates that the diffusion geometry is the dominant factor in determining the ionizer response.

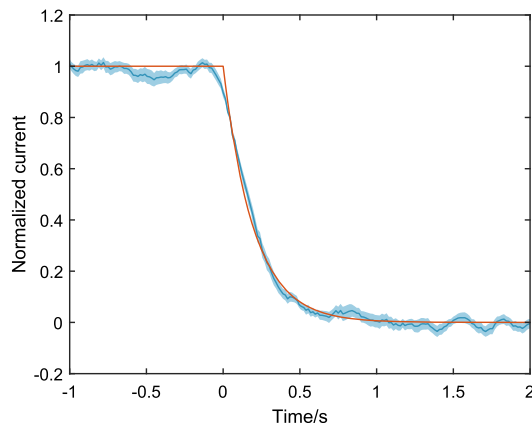


FIG. 16. Plot of the variation of the detected current in a microscope configuration as the beam moves across a sharp edge. The blue line is the mean of 20 normalized experimental scans and the blue shaded region is the standard deviation of the mean. The red line is an exponential step function that interpolates between the initial and final values.

VII. OUTLOOK AND IMPROVEMENT

While the efficiency reported in this work is significantly higher than that available with a commercial detector, there is further scope for improvement. The effects of space charge have not been investigated fully, the ionizer acts as a non-neutral plasma, and the instabilities that arise in electron propagation may disrupt ion extraction.^{41,42} A deeper understanding and control of the space charge inside of the solenoid could lead to both a higher detection efficiency and improvement in stability. Sudden changes in detection efficiency lead to steps in the detector output and can make the collection of data over a long time period difficult.

To minimize the possibility of forming a well in the space charge near the filament,²⁶ the design discussed in the current work uses a filament placed deep inside the solenoid. In previous works, magnetic compression has been used to maximize the electron current passing into the solenoid.^{24,25} Electron beam ion sources (EBISs) have achieved high current densities of $j > 1000 \text{ A cm}^{-2}$,²³ which could improve the ionization efficiency, though that is only achieved at high electron energies. However, electron sources that have energies as low as 60 eV have been reported⁵⁰ so there may be potential in the future for higher currents of electrons being injected into the ionization region using these discussed techniques.

Kalinin *et al.*⁴⁴ demonstrated that additional reductions in the background can be achieved by cooling the system with liquid nitrogen to both suppress electron impact heating and cryo-pump any contaminants. However, electron stimulated desorption would prevent complete removal of the background by cooling.⁵¹

VIII. CONCLUSIONS

In this paper, the design of a high-efficiency detector for low mass species using a solenoidal ionizer has been described. Electrons are generated from a hot cathode and are trapped by electromagnetic fields to create a high electron density for ionization.

Mass filtering was achieved using a 180° permanent magnetic sector and varying ion energies. Ion optics with voltages that scale with ion energy have also been developed to allow mass scans that show that helium is successfully filtered.

A conversion dynode was designed and implemented to convert helium ions into electrons and then multiply the signal using an electron multiplier. The shielding of the entrance of the electron multiplier to external fields is essential to its performance, resulting in the addition of a mesh to the front of the multiplier to be necessary.

Various parameters of the detector were measured to benchmark its performance. The efficiency of the ionizer was measured by an on-axis Faraday cup and shown to be as high as 0.5% for large electron energies despite the complex behavior with respect to the emission current and electron energy. The various backgrounds present were documented and removed until a final background, which is equivalent to a helium flux of only $F_b = (8.7 \pm 0.2) \times 10^6 \text{ s}^{-1}$ entering the detector, was measured. A key result is that the electron energy must be kept below about 100 eV to minimize the background from multiple ionization at $m/z = 4$. Finally, the time constant was shown to be $\tau = (198 \pm 6) \text{ ms}$ as measured on a scanning helium microscope.

While the results presented here are principally concerned with use on a helium microscope, the detector also has wide applicability including measuring other low mass species such as hydrogen.

ACKNOWLEDGMENTS

We acknowledge funding from an FP7 NMP.2012.1.4-3 scheme, project NEMI, Grant Agreement No. 309672 and EPSRC Award No. EP/R008272/1, building on previous research supported by EPSRC Award No. EP/E004962/1. We also wish to acknowledge Gil Alexandrowicz and his group for help in manufacturing the dynode assembly. We would like to thank the expertise of the Cavendish workshop for manufacturing the vast majority of the parts. We would also like to acknowledge Benjamin Davey for his work on developing code for controlling the power supplies and Susanne Schulze for discussions about the manuscript.

DATA AVAILABILITY

A data pack containing the experimental data presented in this paper is available for download from <https://doi.org/10.5281/zenodo.4599730>. The script for modeling gas diffusion through the detector is available from <https://doi.org/10.5281/zenodo.4445536>.

REFERENCES

- 1 J. F. O'Hanlon, *A User's Guide to Vacuum Technology* (John Wiley & Sons, 2003).
- 2 M. Reinhardt, G. Quiring, R. M. R. Wong, H. Wehrs, and J. Müller, *Int. J. Mass Spectrom.* **295**, 145 (2010).
- 3 J. A. Diaz, C. F. Giese, and W. R. Gentry, *J. Am. Soc. Mass Spectrom.* **12**, 619 (2001).
- 4 E. Keppler, V. V. Afonin, C. C. Curtis, A. V. Dyachkov, J. Erö, Jr., C. Y. Fan, K. C. Hsieh, D. M. Hunten, W.-H. Ip, A. K. Richter, A. J. Somogyi, and G. Umlauf, *Nature* **321**, 273 (1986).
- 5 A. Frattolillo and A. D. Ninno, in *2007 IEEE 22nd Symposium on Fusion Engineering* (IEEE, 2007), pp. 1–4.

- ⁶A. Tamtögl, E. Bahn, J. Zhu, P. Fouquet, J. Ellis, and W. Allison, *J. Phys. Chem. C* **119**, 25983 (2015).
- ⁷A. P. Jardine, J. Ellis, and W. Allison, *J. Phys.: Condens. Matter* **14**, 6173 (2002).
- ⁸M. Koch, S. Rehbein, G. Schmahl, T. Reisinger, G. Bracco, W. E. Ernst, and B. Holst, *J. Microsc.* **229**, 1 (2008).
- ⁹P. Witham and E. Sánchez, *Rev. Sci. Instrum.* **82**, 103705 (2011).
- ¹⁰M. Barr, A. Fahy, A. Jardine, J. Ellis, D. Ward, D. A. MacLaren, W. Allison, and P. C. Dastoor, *Nucl. Instrum. Methods Phys. Res., Sect. B* **340**, 76 (2014), part of Special Issue: 20th International Workshop on Inelastic Ion-Surface Collisions (IISC-20).
- ¹¹M. Barr, A. Fahy, J. Martens, A. P. Jardine, D. J. Ward, J. Ellis, W. Allison, and P. C. Dastoor, *Nat. Commun.* **7**, 10189 (2016).
- ¹²P. Witham and E. Sánchez, *Cryst. Res. Technol.* **49**, 690 (2014).
- ¹³A. Fahy, M. Barr, J. Martens, and P. C. Dastoor, *Rev. Sci. Instrum.* **86**, 023704 (2015).
- ¹⁴A. Fahy, S. D. Eder, M. Barr, J. Martens, T. A. Myles, and P. C. Dastoor, *Ultramicroscopy* **192**, 7 (2018).
- ¹⁵M. Bergin, S. M. Lambrick, H. Sleath, D. J. Ward, J. Ellis, and A. P. Jardine, *Sci. Rep.* **10**(1), 2053 (2020).
- ¹⁶M. Bergin, D. J. Ward, J. Ellis, and A. P. Jardine, *Ultramicroscopy* **207**, 112833 (2019).
- ¹⁷A. S. Palau, G. Bracco, and B. Holst, *Phys. Rev. A* **94**, 063624 (2016).
- ¹⁸A. S. Palau, G. Bracco, and B. Holst, *Phys. Rev. A* **95**, 013611 (2017).
- ¹⁹Leybold, Leybold full line catalog (edition 2021): Residual gas analyzer, 330.00.02; accessed January 17, 2021.
- ²⁰M. DeKieviet, D. Dubbers, M. Klein, U. Pieles, and C. Schmidt, *Rev. Sci. Instrum.* **71**, 2015 (2000).
- ²¹E. D. Donets, E. E. Donets, and D. E. Donets, *Rev. Sci. Instrum.* **73**, 696 (2002).
- ²²A. R. Alderwick, "Instrumental and analysis tools for atom scattering from surfaces," Ph.D. thesis, University of Cambridge, 2010.
- ²³G. Zschornacka, M. Schmidt, and A. Thorn, [arXiv:1410.8014](https://arxiv.org/abs/1410.8014) [physics] (2014).
- ²⁴A. R. Alderwick, A. P. Jardine, H. Hedgeland, D. A. MacLaren, W. Allison, and J. Ellis, *Rev. Sci. Instrum.* **79**, 123301 (2008).
- ²⁵D. M. Chisnall, "A high sensitivity detector for helium atom scattering," Ph.D. thesis, University of Cambridge, 2013.
- ²⁶M. Bergin, "Instrumentation and contrast mechanisms in scanning helium microscopy," Ph.D. thesis, University of Cambridge, 2019.
- ²⁷Y. Alkoby, H. Chadwick, O. Godsi, H. Labiad, M. Bergin, J. T. Cantin, I. Litvin, T. Maniv, and G. Alexandrowicz, *Nat. Commun.* **11**(1), 3110 (2020).
- ²⁸O. Godsi, G. Corem, Y. Alkoby, J. T. Cantin, R. V. Krems, M. F. Somers, J. Meyer, G.-J. Kroes, T. Maniv, and G. Alexandrowicz, *Nat. Commun.* **8**, 15357 (2017).
- ²⁹A. Berman, *Total Pressure Measurements in Vacuum Technology* (Academic Press, 2014).
- ³⁰D. J. Douglas, *Mass Spectrom. Rev.* **28**, 937 (2009).
- ³¹IES LORENTZ (software).
- ³²H. Wollnik, *Optics of Charged Particles* (Academic Press, 1987).
- ³³Burle, Channeltron electron multiplier handbook for mass spectrometry applications; accessed January 18, 2021.
- ³⁴N. R. Daly, *Rev. Sci. Instrum.* **31**, 264 (1960).
- ³⁵R. A. Baragiola, E. V. Alonso, and A. O. Florio, *Phys. Rev. B* **19**, 121 (1979).
- ³⁶R. A. Baragiola, E. V. Alonso, J. Ferron, and A. Oliva-Florio, *Surf. Sci.* **90**, 240 (1979).
- ³⁷K. Ohya, T. Yamanaka, K. Inai, and T. Ishitani, *Nucl. Instrum. Methods Phys. Res., Sect. B* **267**, 584 (2009), part of Special Issue: Proceedings of the 17th International Workshop on Inelastic Ion-Surface Collisions.
- ³⁸J. Greenwood, *Vacuum* **67**, 217 (2002).
- ³⁹The final mechanical design was designed in collaboration with Alexandrowicz and his group at the Technion.
- ⁴⁰J. R. de Laeter, J. K. Böhlke, P. De Bièvre, H. Hidaka, H. S. Peiser, K. J. R. Rosman, and P. D. P. Taylor, *Pure Appl. Chem.* **75**, 683 (2003).
- ⁴¹J. R. Pierce, *J. Appl. Phys.* **19**, 231 (1948).
- ⁴²R. C. Davidson, *Physics of Nonneutral Plasmas*, 2nd ed. (World Scientific Publishing Company, London; Singapore; River Edge, NJ, 2001).
- ⁴³J. Martens, A. Fahy, M. Barr, A. Jardine, W. Allison, and P. C. Dastoor, *Nucl. Instrum. Methods Phys. Res., Sect. B* **340**, 85 (2014), part of Special Issue: 20th International Workshop on Inelastic Ion-Surface Collisions (IISC-20).
- ⁴⁴A. V. Kalinin, L. Y. Rusin, and J. P. Toennies, *Instrum. Exp. Tech.* **49**, 709 (2006).
- ⁴⁵H. Tawara and V. P. Shevelko, *Int. J. Mass Spectrom.* **192**, 75 (1999).
- ⁴⁶H. Deutsch, K. Becker, G. Senn, S. Matt, and T. D. Märckd, *Int. J. Mass Spectrom.* **192**, 1 (1999).
- ⁴⁷A. Kramida, Yu. Ralchenko, J. Reader, and NIST ASD Team, NIST Atomic Spectra Database (ver. 5.5.6), National Institute of Standards and Technology, Gaithersburg, MD, 2018, available at <https://physics.nist.gov/asd>, August 27, 2018.
- ⁴⁸T. A. Myles, A. Fahy, J. Martens, P. C. Dastoor, and M. G. Barr, *Measurement* **151**, 107263 (2020).
- ⁴⁹M. Bergin (2021). "Detector-TC-model," Zenodo. <https://doi.org/10.5281/zenodo.4445536>
- ⁵⁰G. Zschornack, J. König, M. Schmidt, and A. Thorn, *Rev. Sci. Instrum.* **85**, 02B703 (2013).
- ⁵¹O. B. Malyshev, R. Valizadeh, B. T. Hogan, and A. N. Hannah, *J. Vac. Sci. Technol. A* **32**, 061601 (2014).